
COMPUTATIONAL STUDY OF NON-ISOTHERMAL SLAG EYE FORMATION AND ITS EFFECTS ON LADLE REFINING

A PREPRINT

Anshuman Sinha
Georgia Institute of Technology
Atlanta, GA 30318
anshs@gatech.edu

Amarendra K. Singh
Indian Institute of Technology
Kanpur, UP 10058
amarendra@iitk.ac.in

August 15, 2023

ABSTRACT

Ladle refining is one of the most important aspects of high-quality steel production. Ladle argon purging which facilitates the refining process also leads to the unwarranted opening of the slag cover known as Slag Eye-opening and has a deleterious effect on the quality of steel. Slag eye-opening has been analysed in past under isothermal conditions whereas ladle refining is a transient and non-isothermal operation. The current study deals with the modelling of slag-eye opening and its effects on ladle refining under non-isothermal conditions. The bubble plume is modelled with the help of Discrete Phase modelling (DPM) coupled with a discrete random walk model for including the particle level turbulence. Temperature-dependent thermophysical properties of slag are obtained from FactSage. Opening of slag-metal interface cools the slag-eye region, which causes changes in the thermophysical properties of the slag phase. These changes are then reflected in the flow characteristics of this complex fluid. The slag's flow profile and eye formation are compared and explained between cold modelling techniques and actual ladle metallurgy. The consequences of changing thermophysical prop during ladle refining manifest in their influence on the overall mass transfer coefficient and the kinetics of desulfurization. This can be achieved without the requirement to solve computationally demanding species transport equations, thereby enhancing the practical efficiency of this approach.

Keywords Multiphase ladle flows, non-isothermal modelling, transient ladle refining, Turbulent mass transfer, Equilibrium thermophysical properties, Slag-eye formation

1 Introduction

Crude steel requires further refining and alloying to obtain steel of desired composition and cleanliness and refining of steel through one or more secondary steelmaking such as ladle refining, RH degassing etc. In the ladle refining process, inert gas, usually argon, is purged into the molten metal bath from the bottom through tuyeres or porous plugs. One of the important refining operations is the ladle furnace (LF) refining operation, in which argon gas stirring is essential in determining and improving the quality of liquid steel [1]. However, the strong purging conditions required for ladle refining, also lead to some unwarranted disadvantages in terms of opening the slag cover, which is also termed as slag-eye opening. Fig. 1, shows schematics of various ladle operations in a step-by-step manner which leads to the desired final steel composition. Here, we can see the various purging conditions giving rise to the bubble-driven liquid metal plume, which due to its buoyancy-driven momentum, provides the necessary circulations needed for the renewal of the slag metal interface and temperature and composition homogenization of the liquid metal bath. As shown in Fig. 1(e), the slag eye opens the way for the pickup of unwarranted elements like Oxygen, Hydrogen and Nitrogen as well as exposes the hot metal to the ambient for heat loss [1, 2]. Hence, minimising slag eye-opening is essential, and a proper understanding of its effects on the overall refining process is important. The understanding of flow fields and changing thermophysical properties pertaining to the interfacial region (as shown in Fig. 1(f), due to the corresponding

heat loss during the refining process helps in quantifying the slag eye size and also provides an insight towards the efficiency of the interfacial refining reactions.

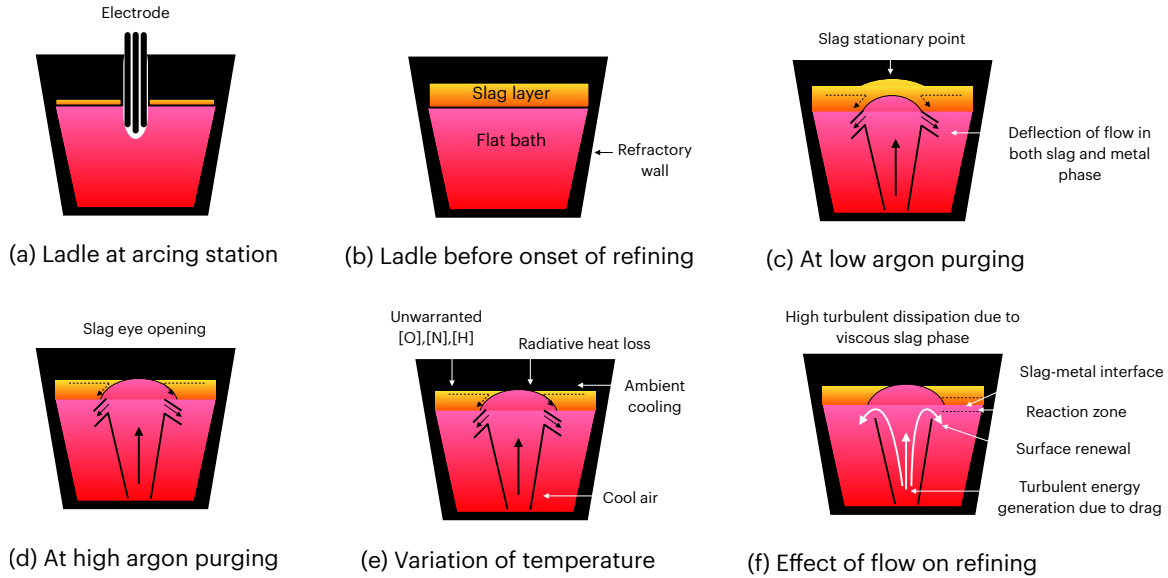


Figure 1: Schematic of step-by-step process flow taking place in the ladle furnace from flat bath condition after EAF/BOF operations to highly turbulent refining condition at the ladle furnace operation unit.

Over the past few decades, many experimental studies and measurements have tried to study the flow field and slag eye formation in view of dynamic similarity in the gas-stirred ladle [3–9]. These experiments were done on cold water models with an overlying oil phase depicting the slag phase. These experiments were conducted with variable bath heights and air flow rates in order to study their effects on slag eye radius and flow properties. The experiments provide quality data for the validation of complex multi-physics mathematical models. Most of the work [10–17] related to non-isothermal studies in the ladle has been done in order to quantify the heat losses during the ladle furnace operations. While these models successfully predict the contribution of various factors towards heat loss, they don't present a study on the effects of these on flow fields or refining conditions. Gonzalez et. al. [18] studied the thermal and chemical homogenization using argon injection sequences with a non-isothermal 4-phase 3D mathematical model. They assumed the thermophysical properties to be held constant throughout the transient simulation, due to which the effects of these parameters could not be studied. Along with the extensive experimental studies, there have been, many physical and numerical modelling studies [19–26] conducted to study the fluid flow behaviour and open-eye formation in the gas-stirred ladle. Over the past decade, the studies were mainly focused on investigating the effect of gas flow rate on the open-eye formation, and relatively few studies on the effect of slag properties (density, dynamic viscosity and upper layer thickness) on the open-eye size through both physical and numerical modelling, the topic which we have taken up as a central theme to our present work.

Furthermore, few investigations in the past have included the effects that the top slag layer has on flow properties [27–31]. Most of these works have reported the effects of these properties on mixing time and have done parametric studies of argon flow rate, bath height, nozzle position, on homogenization of the bath. All these models do not incorporate the transient behaviours of slag phase properties via incorporating equilibrium chemistry models and it's the corresponding effect on the composition of the bath. Ramasetti [32] tried to explain the effects of slag properties on slag eye area with the help of multiple experiments and CFD models with various top layer fluids in a cold model setup, but did not model the transient behaviour of the slag phase in non-isothermal conditions. While work from Jonson ([33, 34]) implements the 2D transient model for slag's properties in a ladle but did not discuss any results pertaining to the transient effects of slag properties on fluid flow, slag eye or the refining process in the ladle.

Table 1: Dimensions of the ladle used in the current work.

Weight (kg)	Density (kg/m ³)	Volume (m ³)	λ_1	λ_2	Height (m)	Diameter (μ m)
120000	7890	15.23	1.8	1.16	2.378	2.64

The present work investigates the effects of the non-isothermal condition of ladle refining which has not yet been addressed in the context of ladle furnace refining and shows the importance of these transient effects on refining after being validated by industrial experimental results. The work focuses on modelling gas-agitated multiphase fluid flow inside the ladle and describes the phenomenon of ladle slag eye formation under non-isothermal conditions which affects the thermophysical and flow properties of the slag phase and finally the refining of molten steel. A 3-Dimensional Multiphysics Eulerian-DPM coupled model is set up with varying thermophysical properties of the slag phase according to the thermodynamic relations. The application of the current model is presented in view of the effects of external argon purging on fluid flow conditions and the overall ladle refining process which can be used directly for industrial application or can serve as a digital twin to make surrogate models for fast model predictions. The work concludes that the non-isothermal modelling presents a more accurate prediction of refining behaviours with increasing rates of desulfurization at higher gas flow rates. Our results show the slowing down of mass transfer phenomena with time as a result of the transient thermochemical behaviour of the ladle during operation. The work opens the door to better and more accurate parametric optimization of the process variables in order to increase the productivity of the metallurgical plants. The application of this is shown with respect to ladle desulfurization by our model in the result section (Section 5), which can be opted for industrial use with appropriate scaling.

2 Problem description

The steel ladle in the current model as described in Table 1, operates with a central porous purging unit for argon purging. The use of a central porous plug gives the advantage while studying the effects of flow properties on slag eye formation and ladle refining-related phenomena. This is taken so, to ensure that none of the spatial-temporal variations in the slag phase occurs due to off-centric purging. The ladle is set for refining after the primary steelmaking operation.

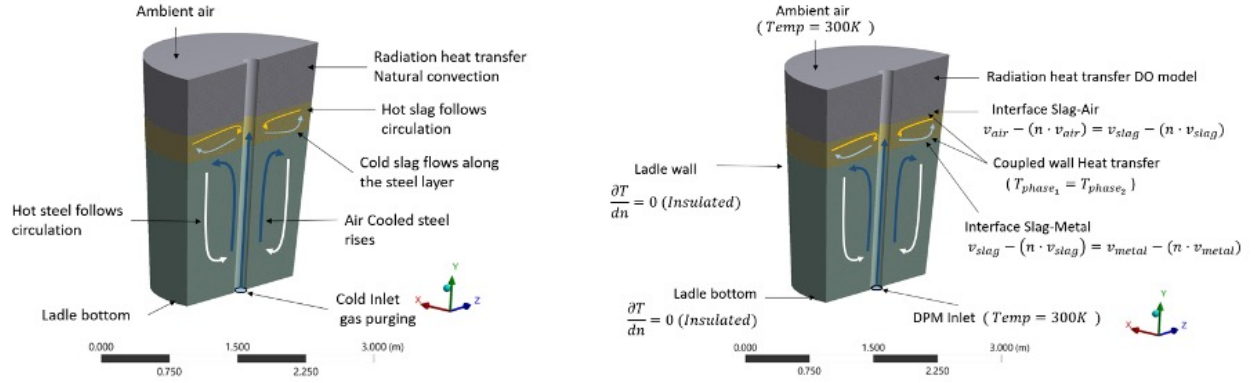


Figure 2: Shows the various boundary conditions and their implementation. (a) Physical boundary conditions and (b) their mathematical interpretations.

The physical description of the problem is described in Fig. 2(a). The various parts of the ladle furnace, along with its components are shown in the figure. The outward tapered ladle consists of liquid steel with overlying slag in the ambient environment. A central purging nozzle is used in order to provide necessary flow circulation with argon gas. The liquid steel and slag system is exposed to cold ambient and argon gas which gradually cools the content of the ladle and thermal gradients develop inside these phases. The thermophysical parameters and interfacial tension between the continuous phases is described in Table 2 and Table 3. The argon flow in the current work is assumed to be in the form of discrete bubbles, the properties of which are described in Table 4 and the properties of DPM Inlet as shown in Fig. 2(b) is described in Table 5.

The physical model is converted into a mathematical form in order to solve the interest variables. The fundamental first step towards this solution procedure is to discretize the domain of interest into several small and strategically shaped domains called cells. Moreover, the stencil which is used to discretize the domain into cells is called mesh.

Table 2: Physical parameters for the simulations [32]

Physical properties at 1873K	Value	Unit
Density of liquid steel	7880	kg/m^3
Viscosity of liquid steel	0.0055	$Pa\ s$
Density of slag	3500	kg/m^3
Viscosity of slag	0.104	$Pa\ s$
Thermal conductivity of slag phase [35]	0.115	$W/m/K$
Thermal conductivity of steel phase [36]	320	$W/m/K$
Density of Argon	0.8739	kg/m^3
Viscosity of Argon gas	2.261×10^5	$Pa\ s$

Table 3: Surface tension modelling between continuous phases [32]

Physical properties at 1873K	Value	Unit
Steel-air	1.82	N/m
Steel-slag	1.15	N/m
Density of slag	0.58	N/m

In the above-described problem, meshing is to be given proper attention as multiple physics are taking place in the domain, which may have different and competing requirements of cell sizes for accurate prediction. A full 3D model is constructed to understand the behaviour and associated flow field and the corresponding formation of the slag-eye. The random walk turbulence model for DPM modelling limits the applicability of the axisymmetric condition in the modelling sense. Moreover, the temperature loss caused by the slag eye is highly dependent on the curvature of the exposed molten metal and slag surfaces due to the inclusion of radiation heat transfer models. Assuming an axisymmetric model would lose out on these details and would not give an accurate picture of non-isothermal conditions.

The set of assumptions have been made in the present calculations, which are as follows:

1. The geometry of the ladle is assumed to be tapered cylindrical, as mentioned in various previous literature. The dimensions are calculated based on (the ' $l = H/r$ ' ratio, ladle tonnage (W), and taper angle (or $l = r_2/r_1$ ratio)) as given in Table 1.
2. At the start of the simulation, the liquid steel bath and the slag phase in the ladle are assumed at a constant and homogenized temperature of 1873K (1600 °C).
3. Liquid steel, slag, and argon have been considered to behave like incompressible Newtonian fluids. Argon, being gas, is compressible. However, in the context of ladle processing, researchers in the past have treated argon as both compressible [37, 38] as well as incompressible [27, 39–42]. We have treated argon as an incompressible fluid as the flow conditions in the ladle have a low Mach number, and the compressibility factor for argon is acceptably small for the pressure stratification due to the height of the liquid steel.
4. The ambient is assumed to be at 300 K. The heat transfer from the ladle is only considered from the top of the ladle. The refractory sidewalls are assumed to be adiabatic as the heat loss from the sidewalls would not significantly affect the change in slag's temperature (T_{slag}).
5. The ladle refining process is articulated with the help of convective mass transfer co-efficient only. The explicit interfacial chemical reaction between steel and slag phase is not considered separately.
6. A full 3D model is constructed to understand the behaviour and associated flow field and the corresponding formation of the slag-eye. The random walk turbulence model for DPM modelling limits the applicability of the axisymmetric condition.
7. The composition of all the phases is assumed to be constant to limit the computation cost of this 3D transient model.

Table 4: Physical parameters of the discrete bubble phase

Physical properties at 1873K	Value	Unit
Bubble Size	4	mm
Bubble density	1.68	g/cm^3
Bubble viscosity	0.001	$Pa\ s$
Surface tension	0.015	N/m

Table 5: DPM particle inlet characteristics

Physical properties at 1873K	Value	Unit
Particle diameter distribution	Uniform	—
Initial velocity	0	m/s
Number of holes	5	—
Injection type	Inlet surface	Normal to surface
Mass flow rate	4.65×10^{-5}	kg/s

3 Numerical modelling

The physical model as described in Fig. 2(b) is implemented in a three-dimensional transient mathematical model for argon gas stirred ladle which accounts for the steel, slag, and argon phases has been developed. A set of Navier–Stokes equations with the incorporation of the volume-of-fluid (VOF) function has been solved to investigate the dynamic behaviour of the three phases. The boundary conditions of the problem statement are shown in Fig. 2(b). The following sets of transport equations [43] are solved.

3.1 Governing equations

Continuity equation

$$\frac{\partial \rho}{\partial t} + \nabla \cdot (\rho \mathbf{v}) = 0 \quad (1)$$

Momentum equation

$$\frac{\partial \rho}{\partial t} + \nabla \cdot (\rho \mathbf{v} \mathbf{v}) = -\nabla p + \nabla \cdot [\mu_e (\nabla \mathbf{v} + \nabla \mathbf{v}^T)] + \rho \mathbf{g} \quad (2)$$

where p is the local pressure, \mathbf{g} is the acceleration due to gravity, \mathbf{v} is the local velocity and μ_e is the effective viscosity. The effective viscosity is calculated as the sum of dynamic and turbulent viscosities.

Energy equation

$$\frac{\partial \rho}{\partial t} + \nabla \cdot (\mathbf{v} [\rho E + p]) = \nabla \cdot \left[k_{eff} \nabla T - \sum_j h_j \mathbf{J}_j + \boldsymbol{\tau} \cdot \mathbf{v} \right] + S_E \quad (3)$$

k_{eff} is effective conductivity of the medium in which energy is to be propagated, h is enthalpy or the heat content of the medium, S_E is the source term which can be used to define external sources like heating elements. The term $E = h + \frac{p}{\rho} + \frac{|\mathbf{v}|^2}{2} + k_{eff}$ is defined as the net energy of the system as defined in equation Eq. 3

DPM equation

$$\frac{d\rho}{dt} = F_D (\mathbf{u} - \mathbf{u}_p) + \frac{\mathbf{g} (\rho_p - \rho)}{\rho_p} + \mathbf{F} \quad (4)$$

where \mathbf{F} is an additional acceleration (force/unit particle mass) term, $F_D (\mathbf{u} - \mathbf{u}_p)$ is the drag force per unit particle mass and $F_D = (18\mu/24\rho_p d_p^2) (C_D Re/24)$, and corresponding $Re = \rho d_p |\mathbf{u} - \mathbf{u}_p| / \mu$ is the Reynolds number with respect to the continuous phase. Here, \mathbf{u} is the fluid phase velocity, \mathbf{u}_p is the particle velocity, ρ is the fluid density, ρ_p is the density of the particle, and d_p is the particle diameter. Re is the relative Reynolds number.

Radiation transfer equation The contribution to heat transfer from radiation was calculated by using the non-grey discrete ordinates (DO) radiation model. In this model, we compute the heat transfer in the direction of heat transfer rays \mathbf{s} , along this direction the radiative transfer equation for spectral intensity $I_\lambda(\mathbf{r}, \mathbf{s})$ can be written as follows:

$$\nabla \cdot I_\lambda(\mathbf{r}, \mathbf{s}) \mathbf{s} = (a_\lambda + \sigma_\lambda) I_\lambda(\mathbf{r}, \mathbf{s}) + a_\lambda n^2 I_{b\lambda} + \frac{\sigma_s}{4\pi} \int I_\lambda(\mathbf{r}, \mathbf{s}') \phi(\mathbf{r}, \mathbf{s}') d\Omega' \quad (5)$$

The four terms in Eq. 5 represent the rate of increase in radiation intensity, loss by absorption and out-scattering, gain by emission, and gain by in-scattering, respectively. The present study applies the grey-band model for eight discrete bands [45] and uses the averaged absorption coefficient for each wavelength band. The absorption coefficient a_λ in Eq. 5 was estimated from the measured transmittance and reflectance [35, 43].

Table 6: Composition of the slag used in our current work [45]

Al_2O_3 ([wt%])	SiO_2 ([wt%])	CaO ([wt%])	MgO ([wt%])	Temp. (K)	Viscosity (Pa s)	density (kg/m^3)
120000	7890	15.23	1.8	1.16	2.378	2.64

Turbulence $\kappa - \epsilon$ model equations

$$\frac{\partial}{\partial t} (\rho \kappa) + \nabla \cdot (\rho \kappa \mathbf{u}_i) = \nabla \cdot \left(\left[\mu + \frac{\mu_t}{\sigma_k} \nabla(\kappa) \right] \right) + G_k + G_b - \rho \epsilon - Y_m + S_k \quad (6)$$

Dissipation equation

$$\frac{\partial}{\partial t} (\rho \epsilon) + \nabla \cdot (\rho \epsilon \mathbf{u}_i) = \nabla \cdot \left(\left[\mu + \frac{\mu_t}{\sigma_k} \nabla(\epsilon) \right] \right) + C_{1\epsilon} \frac{\epsilon}{\kappa} (G_k + C_{3\epsilon} G_b) - C_{2\epsilon} \rho \frac{\epsilon^2}{\kappa} + S_e \quad (7)$$

Where the terms G_k and G_b represent the generation of kinetic energy due to turbulence from the mean velocity gradient and the generation of kinetic energy due to turbulence from the effects of buoyancy, respectively. Similarly, S_k and S_e are sink terms in the respective equations which counter the generation of energy or dissipation by eliminating the energy to other smaller scales of motion. $\mu_t = \rho C_\mu (\kappa^2 / \epsilon)$. The turbulent viscosity is calculated as μ_t by using the ‘ κ ’ and ‘ ϵ ’ from Eq. 6 and Eq. 7 respectively. In these equations many constants are used whose values are as follows: $C_{1\epsilon} = 1.44$, $C_{2\epsilon} = 1.92$, $\sigma_k = 1.0$, $C_{3\epsilon} = 1.0$, and $\sigma_\epsilon = 1.3$ [36].

Volume-of-Fluid (VOF) fomulation The VOF formulation assumes that the various phases present in the system are not interpenetrating. While the interaction between the phases is based on the modelling of the interfaces between the phases. Therefore, each phase in a cell is represented by its volume fraction. Volume fractions are derived by solving the continuity equation for each phase given in equations below.

$$\frac{\partial \alpha_q}{\partial t} + (\mathbf{v} \cdot \nabla) \frac{\partial \alpha_q}{\partial t} = 0 \quad (8)$$

$$\alpha_g + \alpha_l + \alpha_s = 0 \quad (9)$$

where α is the volume fraction value of g , l , and s for argon gas, steel, and slag phases.

$$\rho = \alpha_g \rho_g + \alpha_l \rho_l + \alpha_s \rho_s \quad (10)$$

The density of the mixture is calculated by Eq. 10 and used in Eq. 1–4 and Eq. 6–7.

Equilibrium model for thermophysical properties The most important factors governing the rheological properties of slag are its density ρ_{slag} , viscosity of the liquid phase η_{eff} and the fraction of crystals ϕ . For the equilibrium model, we have considered the following slag system is shown in Table 6 for our study. The equilibrium phase diagrams along with the apparent viscosity both are calculated by the ‘Equilib’ and ‘Viscosity’ packages respectively of FactSage software [44].

Later the data from these two packages are used to calculate the density and viscosity of the slag phase at various slag operating temperatures, in order to get the relations between temperature and effective viscosity from Eq. 11 and temperature and slag density from Eq. 12.

The slag’s thermophysical properties are strongly dependent on the phase composition of the slag phase at the different operating temperatures. FactSage software [44] is used to obtain the solid fractions of the above slag composition at different temperatures.

Slag viscosity formulation The viscosity of the slag strongly depends on the melt composition, including the amount of constituent solid particles and the temperature of the slag phase. The viscosity of the complete slag phase is estimated in terms of the effective viscosity of melts containing all kinds of particles with the Einstein-Roscoe equation. [42]

$$\eta_{eff} = \eta_m \left(1 - \frac{\phi}{\omega} \right)^{-2.5} \quad (11)$$

Table 7: Optimized parameter values of $V_{i,R}$ and $\partial V_i/\partial T$ [47]

Components	$V_{i,R}(1773K)(m^3mol^{-1})$	$\partial V_i/\partial T(m^3mol^{-1}K^{-1})$
SiO_2	26.312×10^{-6}	0.740×10^{-9}
Al_2O_3	28.700×10^{-6}	10.108×10^{-9}
CaO	18.0312×10^{-6}	1.014×10^{-9}
MgO	12.076×10^{-6}	0.683×10^{-9}

Table 8: Slag thermophysical properties of viscosity and density for the steel refining operating temperatures

Temp (°C)	$\mu_{app}(Pa\ s)$	Solid wt. (g)	Solid frac.	Ein. Richoe Coeff.	$\eta_{eff}(Pa\ s)$	$\rho \times 10^3 (kg/m^3)$
1600	0.083	1.389	0.014	1.036	0.086	1.883
1580	0.091	1.235	0.012	1.032	0.094	1.946
1560	0.101	1.8	0.018	1.046	0.106	2.010
1540	0.112	2.217	0.022	1.058	0.118	2.073
1520	0.125	2.54	0.025	1.066	0.133	2.136
1500	0.139	2.735	0.027	1.072	0.149	2.200
1480	0.155	2.973	0.030	1.078	0.167	2.263
1460	0.174	3.198	0.032	1.085	0.189	2.327
1440	0.196	3.412	0.034	1.091	0.214	2.390
1420	0.221	10.807	0.108	1.331	0.294	2.453
1400	0.25	19.469	0.195	1.718	0.430	2.517
1380	0.283	25.081	0.251	2.058	0.583	2.580
1360	0.322	30.775	0.308	2.508	0.808	2.643
1340	0.368	42.198	0.422	3.937	1.449	2.707
1320	0.422	49.798	0.498	5.600	2.363	2.770

Where η_{eff} is the effective viscosity of the slag phase with a volume fraction ϕ of crystals, and η_m is the viscosity of the liquid part of the slag. The parameter ω corresponds to the crystal fraction or the solid phase, at which a transition of the system to a rigid state occurs. This parameter is obtained from optimised experimental data. Researchers in the past have used values between (0.6 – 1) for ranging slag systems. [21, 46] We have used the value of 0.6 for our current simulations. Effective viscosity in a slag system majorly depends on the phase fraction of the corresponding phases. The monoxide phase is responsible for the solid fraction of the slag. And thus has a certain amount of solid associated with it. Further, this equilibrium model was used to calculate the solid fraction which comes out to be 0.014 as shown in Table 8.

Slag density formulation In any multiphase system, the density is found to be proportional to the reciprocal of the molar volume of the components. In the current work, we have implemented the density of molten slag in the following manner as represented by Eq. 12.

$$\rho_{slag} = \frac{X_i M_i}{V_m} \quad (12)$$

where ρ is the density of the slags, X_i is the mole fraction of component i , M_i is the molar mass of component i , and V_m is the molar volume of slag. The molar volume of slag was calculated according to molar volume of pure components $V_m = X_i V_i(T)$. The component molar volume $V_i(T)$ as shown in Table 7 for the various components was further expressed in form of linear dependence of temperature in Eq. 13:

$$V_i(T) = V_{i,R} + (T - T_R) \frac{\partial V_i}{\partial T} \quad (13)$$

Where $V_{i,R}$ is the partial molar volume of the component ‘ i ’ at reference temperature T_R , and $\partial V_i/\partial T$ is the thermal expansion coefficient of component ‘ i ’ as shown in Table 7. The viscosity and density of slag phase for the above slag composition in the operating slag temperature are calculated using the above Eqs. 11–13. The results are tabulated in the following Table 8. The Effective viscosity (η_{eff}) is plotted and fitten with a least square error trendline of a polynomial function with a degree 5 exponent in the Fig. 3. Similarly, for the various discrete temp, slag’s density (ρ_{slag}) was calculated and then interpolated to build the UDF for density and viscosity. As shown in the Fig. 3 where slag density against temperature u relation in Eq. 13.

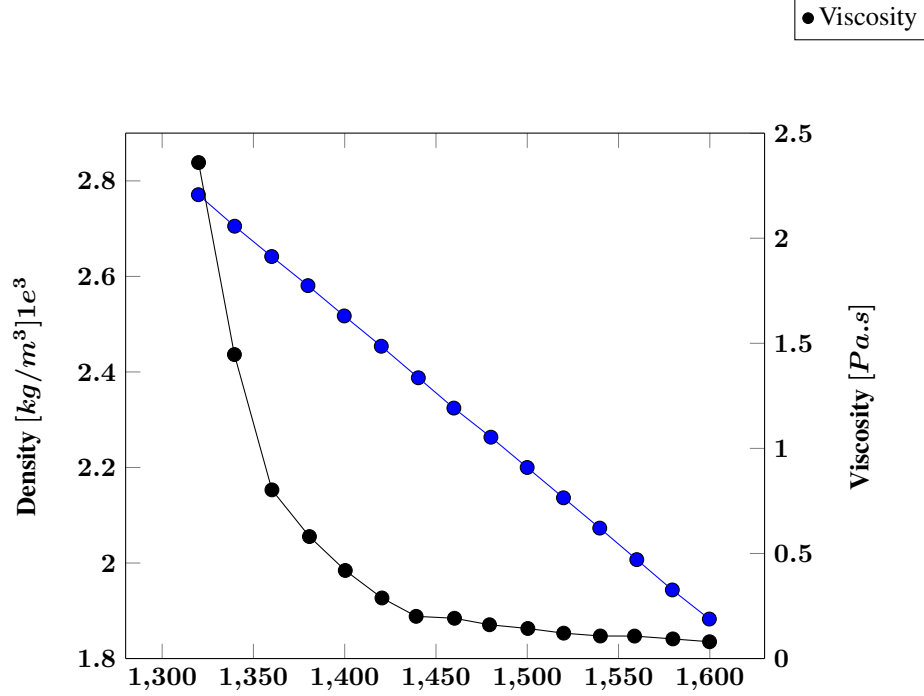


Figure 3: Plot of density considering the temperature dependent Molar volume of constituent slag phases.

Mass transfer in refining ladle The steel-slag interface is a liquid-liquid interface which is continuously subjected to turbulence due to the continuous stirring of the steel ladle. Various turbulence models are there which account for the continuous renewal of fluid elements at the reaction interface and their corresponding mass transfer rates [48]. In this work, we have used the surface renewal model of turbulent mass transfer theory for transfer between two liquids [49]. This new theory is based on the eddy models of turbulence and depends on parameters of turbulence, primarily eddy-viscosity related such that it fits on some solvable equations. Similar to the other turbulent mass transfer models, the ‘Eddy theory’ describes the mass transport of species using turbulent eddies present at the interface of the liquids. This model provides this link between eddy theory and mass transfer by making use of the spectrum of turbulent energy and superimposing it with the mass transfer behaviour of an idealised small eddy motion in the vicinity of the interface. The fluctuating turbulent velocities are assumed to be the dominating field of velocity near the interface.

Following the ‘small eddy model’ we need to define the mass transfer of reacting species across the slag metal interface. For this we define a mass transfer source term, which can be computed as follows in Eq. 14.

$$S_i = m_{pq} = k_{pq} a_i (\rho_{q,e}^j - \rho_q^j) \quad (14)$$

Here S_i represent the general interphase mass transfer source term between phase p and q , and $(\rho_{q,e}^j - \rho_q^j)$ is the potential to this mass transport, with $\rho_{q,e}^j$ being the equilibrium mass fraction and ρ_q^j being the present mass fraction. The same equation (Eq. 14) is used in the Section 5.2 (Eq. 17.) to describe the desulfurization behavior of the ladle. There we will compute the integral of the rate of change of element sulfur due to the interfacial reaction. Further, to relate the fluid flow and mass transfer mathematically by accounting the rate coefficient ‘ k_{pq} ’ written as ‘ k_L ’ (in m/s) we express the following relation in Eq. 15:

$$k_L \propto \left(\frac{\mu}{D}\right)^{-1/2} (\epsilon\mu)^{1/4} \quad (15)$$

The expression for the rate coefficient ‘ k_L ’ is expressed in the above equation. Where k_L is the mass transfer coefficient, ν (m^2/s), is the kinematic viscosity of the metal phase, D (m^2/s) represents the Molecular diffusivity of concerned transporting species in the metal phase and ϵ (m^2/s^3) the kinetic energy dissipation rate of the metal phase by the above lying slag phase. Using the ‘Eddy cell model’ we have the relation between the mass transfer coefficient and turbulent flow variables. The proportionality constant for the above relation is taken to be 0.4, as experimentally determined for various flows. [50] For a crude sense, a high proportionality constant would capture the effects of larger eddies into

mass transfer. In the current work, we assume the diffusivity D of Sulfur in metal is 3.5×10^{-9} constant throughout the process, as the effects of non-isothermal changes are limited in the metal phase. Thus to limit complexities we have assumed a constant metal phase diffusivity. [51]

3.2 Solution procedure

Geometry specifications A highly intensive geometry and meshing is used to describe and discretise the physical geometry, such that the following criteria as well met.

1. The hexahedral mesh in most parts of the geometry is chosen for better computational efficiency,
2. The volume of the cells for the DPM region are selected such that particle loading is not overburdened.
3. The slag-steel interface is finely meshed to capture the numerical shape changes from the VOF method, such that the slag-eye formation is appropriately addressed.
4. The zones with low fluctuations of velocity are coarsely meshed to gain computational efficiency
5. The rectangular porous plug region is adapted with the cylindrical ladle such that low skewness levels are achieved overall.
6. Finally, a multizone method is used for coupling the different zones to achieve proper coupled solution.

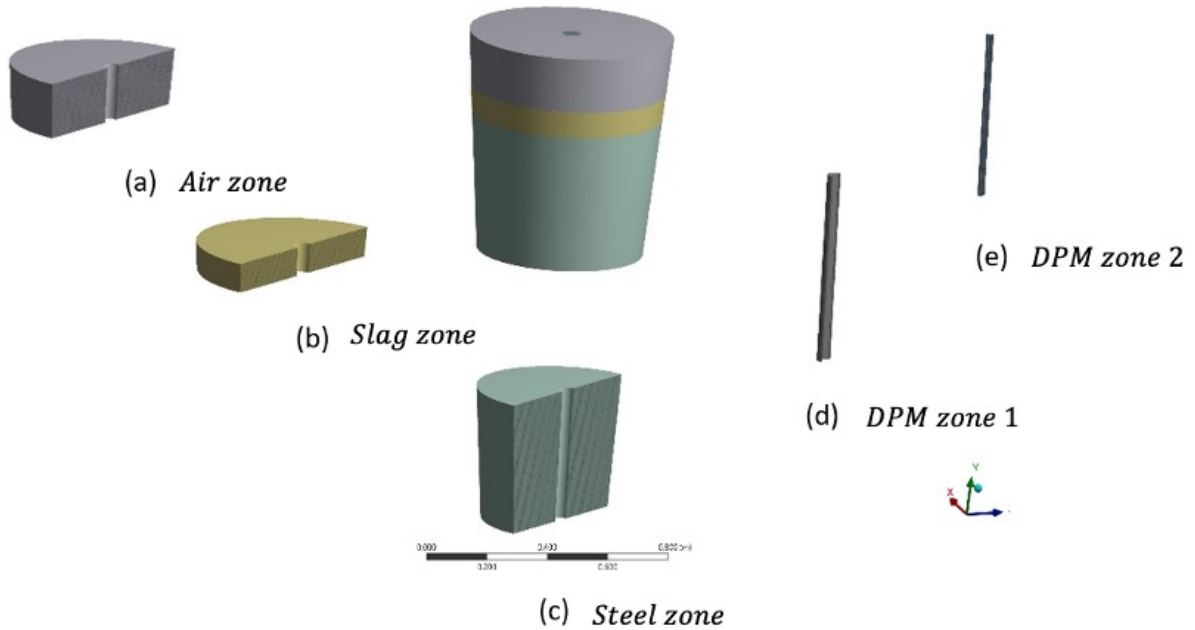


Figure 4: Physical domain converted into components of geometry. The various domains from (a-e) are created in a manner such that an optimum balance between the density of mesh points and features of the flow is observed for computational efficiency.

The geometry was created with the help of five different zones as shown in Fig. 4, The coarse Air zone (Fig. 4(a)) were not much flow was expected, followed by a very fine slag zone (Fig. 4(b)) where high rates of change of velocity vector along with rapid interfacial deformations were expected. This was followed by a medium coarse mesh for the steel zone (Fig. 4(c)), where predominantly large scales of motion were expected in the form of recirculation. Finally in order to efficiently capture the trajectories of the discrete phase particles, a separate zone DPM zone 1 (Fig. 4(d)) with high cell volume was created and adapted with the previous zones using DPM zone 2 (Fig. 4(e)). Fluent 18.0 Mesh building tool is used to create this customised mesh following the above criteria. The details about the mesh quality and sizing are described in Table 5. The final mesh with the given physical domains and detailed mesh structure is shown in Fig. 5.

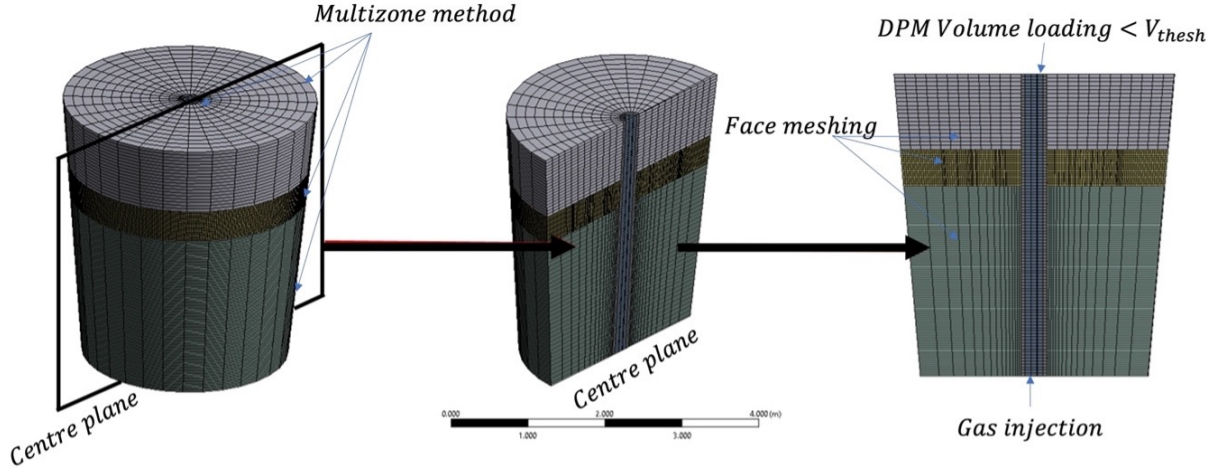


Figure 5: Showing the mesh structure used as stencil to perform the domain discretisation

3.3 Methodology

The governing equations of unsteady state are to be solved on the mesh points which are shown in the previous section. The following numerical methods with First-order Up-wind and PISO algorithm for pressure-velocity coupling were implemented for obtaining the final set of algebraic equations after the governing equations were implemented on the mesh obtained in Section 3.2.

Solution control Under-relaxation factors used in the simulation are: 0.8 for discrete phase source, 0.8 Turbulent kinetic energy, 0.8 Turbulent Dissipation rate, 0.7 for momentum. The rest of the factors are set to 0.8.

Convergence: The convergence for each time step for the continuum phase and discrete phase solver is attained when the error in flow variables in successive iterations comes below $1e-5$.

Time-step control: Using fixed time stepping method at 0.001 sec 'Time step size'. The DPM particles ejection from the inlet are set for each continuum phase time step.

3.4 Solution algorithm

The given problem is solved by implementing a coupled Eulerian-Discrete solution, where continuum phases like steel phase, slag phase and air phase are modelled by Eulerian modelling while the discrete phases like Argon gas bubbles (from bottom Argon gas purging) are modelled with discrete phase modelling. The coupling is achieved with the help of source and sink terms. The current solution is modelled with a 2-way coupling approach as shown in Fig. 6, where the interaction forces are computed separately for both the phases in an explicit manner.

Solution algorithm The coupled equations of motion for incompressible isothermal multi-fluid flow are solved using a 2 way Eulerian-DPM coupled approach. The UDF implementation is linked with a 1 way explicit coupling with the Equilibrium solver. The solution algorithm for advancing the solution of the flow field from the first time-step is as follows:

1. Initialise the solution with the initial conditions as given in the problem description (Section 2). Compute new density and viscosity distributions with the help of User defined function and initial conditions.
2. Compute the flow and pressure fields (v, p) at the discretised mesh points using the continuity and momentum equations with the help of the methods described in Section 3.2. Solve for the energy and turbulence variables E , k and ϵ with the help of energy and turbulence equations and the flow fields computed in the above step.
3. Compute the interaction forces like Drag and buoyant forces and send these forces to the discrete phase model equations as a source and sink terms.

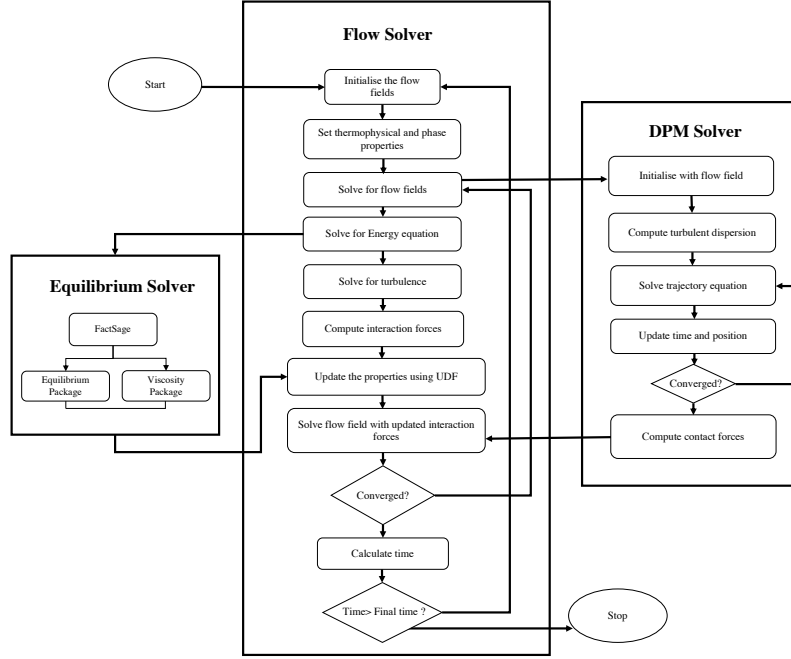


Figure 6: The Solution algorithm used in the current problem.

4. Solve the trajectory equation for the discrete phase particles till convergence of 10^{-5} for calculating variables is reached. Afterwards, recompute the drag force. Send this updated drag force back to the continuum flow solver.
5. Use the updated interaction forces and recompute the continuum phase flow variables till convergence is reached.
6. Update the viscosity and density for the next time-step using the user-defined functions for viscosity and density and update flow time.
7. Return to step 2 while using the current solution for flow fields and phase properties as initial conditions.
8. Stop after reaching the final time.

4 Validation

The numerical model which has been presented in Section 3 has been validated with the experimentation done by previous publications [8]. Here, an acrylic container vessel was used to simulate the slag eye formation, it was used to experiment with a steel ladle with the ladle being scaled down to 1/10th. Air was injected through a central nozzle unit, which was 3mm in diameter, The experimental ladle was of height 50 cm and the diameter was calculated to be 42 cm. A schematic of the experimental apparatus is discussed in the literature of the paper [8].

The eye area for various operating conditions was obtained from video recordings in the experiment. The eye area fluctuates over time due to the stochastic nature of the bubble rising in the plume. The same experiment was simulated with the existing model parameters for the water and oil phase and the air bubbles prepared as DPM particles. The results of the present model are consistent with those of the experiments as shown in [8]. However, we observe low predictability of the results at low flow rates (as shown in Fig. 8, which could possibly be due to the higher number of discrete phase particles in a single volume at low flow rates, thereby decreasing the efficiency of the solver to handle and track the particle movements well. The ANSYS Fluent solver mentions this as a remark in the user manual [52], that the percentage of DPM particles in any given cell should not exceed 15% by weight. Otherwise, the solution to the continuity equation of the continuous phase suffers. However, at a more significant flow rate, the particles travel faster from one cell to another, and thus, it becomes easier for the solver to handle these particles.

Capturing the various physics in the ladle furnace, we need to systematically present the results to link them in sequence with the physics.

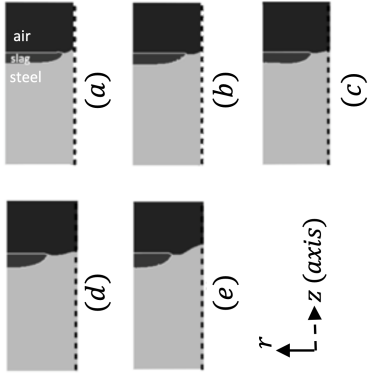


Figure 7: Validation part Effect of flow rate on eye size with (3 cm oil) for ($H/D = 0.75$)

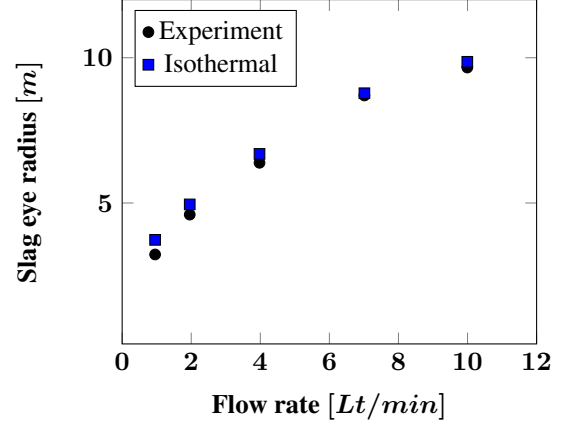


Figure 8: Comparison between experimental and modelled result

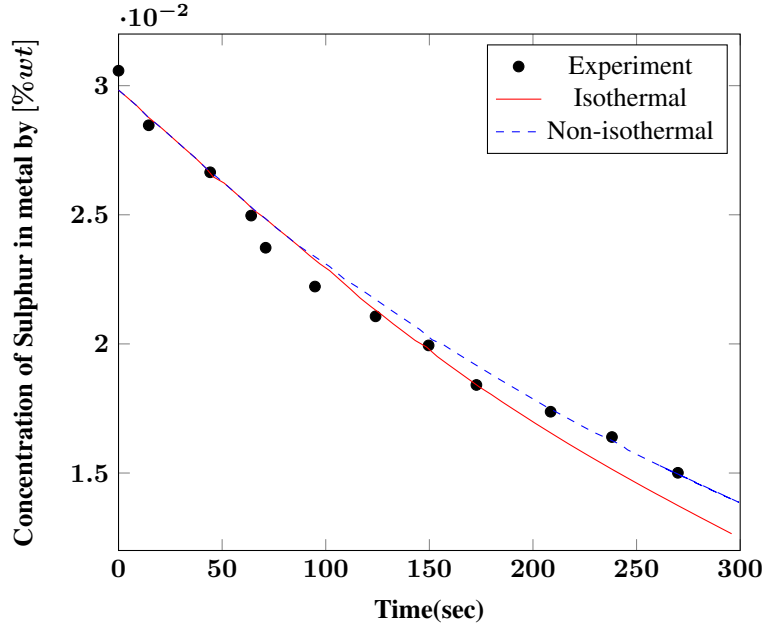


Figure 9: Comparison of isothermal and non-isothermal model with respect to experimental data [33]

In this part, the current numerical model for non-isothermal ladle refining has been validated against previous experimental work from [33]. Here we have modelled the same experimental setup numerically and tried to get the results for the case with the same geometrical configurations of the ladle. The Sulfur slag metal reaction was taken to be a mass transfer phenomenon and was demonstrated in the later Section 5.2. The physical parameters, and initial and boundary conditions for steel and slag are taken the same as in the experiment. And a bath flow rate of 80 Nl/m is implemented in a bath of 2.1 m , with the initial Sulfur concentration being $0.031\% \text{ wt.}$.

In Fig. 9 we observe the desulfurization behaviour of both the Non-isothermal and isothermal models with respect to the experimental measurements. The experimental results match well with our current Non-isothermal model, while the isothermal model tends to overpredict the results, especially in the later period of desulfurization, where the effect of non-isothermal conditions starts to take major effects. The study here presents the validation of this model. Moreover, we also observe that the non-isothermal model achieves great accuracy without the need of any complex species transport or surface reaction formulation, which supports our use of mass transfer driven de-sulfurisation.

5 Results and discussions

The results of the current work are discussed in three separate sections, which deal with aspects of ladle refining in a step-by-step manner.

- Slag-eye formation during ladle processing in the non-isothermal modelling framework. How slag eye gets formed.
- Results related to non-isothermal ladle conditions and how non-isothermal modelling affects slag-eye formation
- Effects of slag eye formation on ladle refining in non-isothermal condition.

5.1 Slag-eye formation in steel ladle:

The purging of inert gas through the bottom tuyere forms a buoyant plume of the gas-liquid mixture. The buoyant plume rises with upward momentum. In strong purging conditions, the upward momentum of the plume displaces the overlying slag phase and forms a slag eye-opening. The upward-rising gas bubbles move out of the metal phase and get into ambient air leaving the plume behind it, as shown in Fig. 10(c). The plume then loses its upward driving force due to the downward pull by gravitational forces and thus turns in a downward direction. This turning of the plume also drags the adjacent slag phase and sets up a recirculating motion in the slag phase, as shown in Fig. 10(a) and Fig. 10(d). The velocity contour plot of the slag phase velocity as shown in Fig. 10(a) shows the velocity profile in the slag region only. Here, we observe that most of the flow occurs in the lower region of the slag phase which is in contact with the metal phase as it is directly in contact with the lower moving metal phase! Apart from that, the changing thermophysical properties of the slag phase also favour this region to be at the maximum velocity which is discussed in the later section.

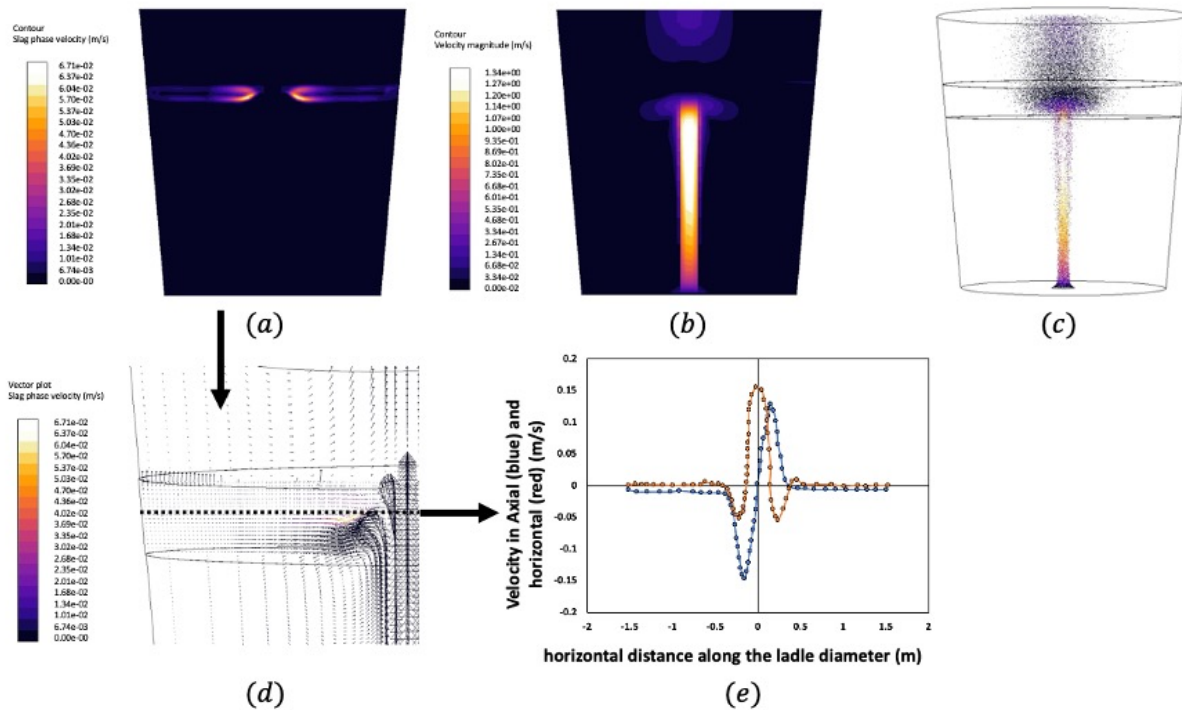


Figure 10: The contour of velocity profiles at the centre plane where (a) shows the velocity profile in the slag phase only and (b) describes the continuous phase mixture velocity pertaining in the ladle (c) DPM particle in the domain marked by the velocity colourmap. Buoyancy-driven argon bubbles are modelled as DPM particles moving in a continuous phase. (d) The velocity vector profile in the slag region colour mapped to the range of slag velocity. (e) A plot of axial and horizontal velocity is shown on the ladle diameter line (the asymmetry due to bubble-induced turbulence is observed) at ladle height = 2.45m.

Fig. 10(b) shows the primary phase (metal phase) flow profile due to the two-way coupling of the discrete phase (argon bubbles) with the primary phase. The flow profile in the ladle due to the rising plume forms a somewhat conical shape because of the random collisions that occur in the bubble plume, increasing the dispersion of the bubble. And the conical shape of the plume is mainly attributed to two factors. Firstly, stochastic turbulence in the bubble, and secondly,

the downward motion or resistance provided by the slag phase, which deflects and spreads the rising liquid at the edges of the plume. The bubbles (discrete phase particles) in Fig. 10(c) then move upwards in the ladle and pull the liquid with them, while the bubble then moves upwards through the slag; The primary phase collides with the liquid slag phase and then recedes towards the walls. Afterwards, the continuous phase moves downward, creating circulation inside the ladle, as can be seen in the vector plot of the velocity profiles in Fig. 10(d). The circulations in the slag phase result in the asymmetric velocity plot in the horizontal direction (radial) to the axis. The slag phase moves downwards due to recirculation as can be observed from the axial velocity plot in Fig. 10(e). This detailed description of the flow field pertaining to both slag and metal phases helps in understanding the effects which arise due to the inclusion of non-isothermal conditions and is further discussed in the later sections of this paper.

5.2 Results related to Non-isothermal ladle conditions

Effect of Non-isothermal ladle conditions on slag eye formation

At the onset of ladle processing, Argon purging is performed at varying rates depending upon the timeline pertaining to the ladle processing, such as a low purging rate for mixing, a high rate of purging for de-S, etc. The argon purging brings about the effect of relatively cooler gas being blown in the hot metal, resulting in inevitable temperature loss. Moreover, as discussed in the previous section the upward-rising buoyant plume also causes the creation of slag eye opening during high purging. This way the hot metal is exposed to the ambient air at cooler temperatures, and heat losses start to occur from this open eye.

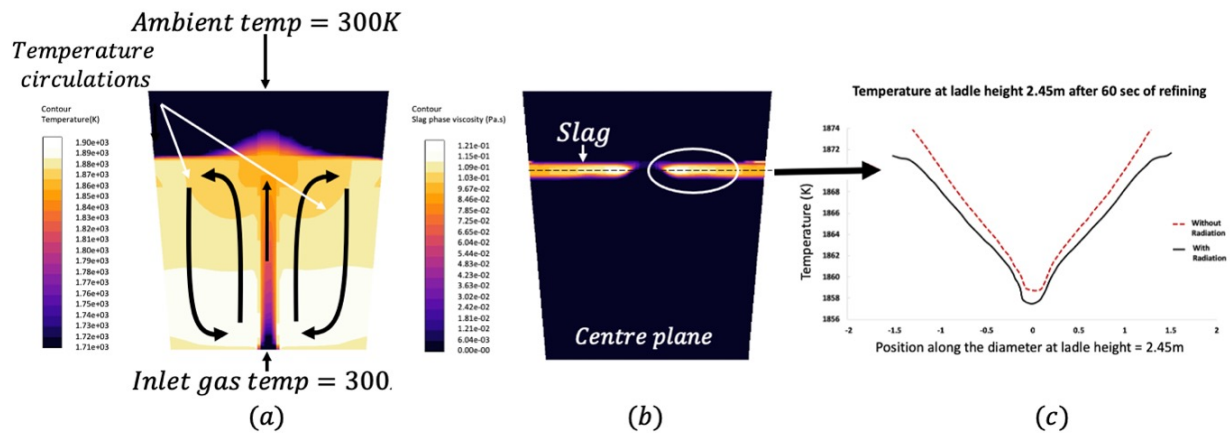


Figure 11: (a) The temperature distribution of the mixture phase in the ladle (clipped to range 1900K-1700K), the temperature distribution contour is after 60 sec from the start of the simulation.(b) Slag viscosity variation in the slag eye region and (c) the plot of the corresponding temperature at ladle height = 2.45m marked by the dashed line after 60 sec from the start of the simulation.

We start our discussion with the results for the total temperature profile within the ladle, as we can see from Fig. 11(a). The coldest region exists at the ladle bottom due to cool argon purging, and next up we see the region, which is near the open slag eye. It can also be judged from the implications of the radiative flux model, as the element's radiative flux contribution to another region in the molten metal is almost uniform and thereby can't cancel out each other, while the elements near the slag open eye region have less radiant flux coming from the elements from the top (i.e., the ambient) than what it is emitting from itself. The effect of including this radiation model can be seen in Fig. 11(c), where the temperature profile comes out to be lower than the model with a no-radiation model.

The effect of the temperature is reflected upon the thermo-physical properties of the materials and in turn the flow conditions in the ladle. As shown in Fig. 11(b) the viscosity of the slag phase is varying in the ladle as the temperature continuously drops in the ladle due to the reasons described in the previous paragraph. We see a marked viscosity increase in the region near the slag eye region, this can be well related to the temperature profile on the line in the inter-slag region. This viscosity increase can be well attributed to the change in the flow profile in the slag and the interfacial region in the metal phase. The results of these changes will be attributed in the next sections where we will relate the flow change effects to the macroscopic effects of refining.

Slag eye area as observed in Fig. 13(a), is one of the most important parameters in ladle processing as discussed in the previous section. The thermophysical properties and the flow regime in the interfacial region particularly near the bubble plume are important for the dimension of the slag eye area. Fig. 13(b) and Fig. 13(c) shows the effect of including the variations in the thermophysical properties on the slag eye. Here we observe a smaller slag eye area when the thermophysical properties are considered.

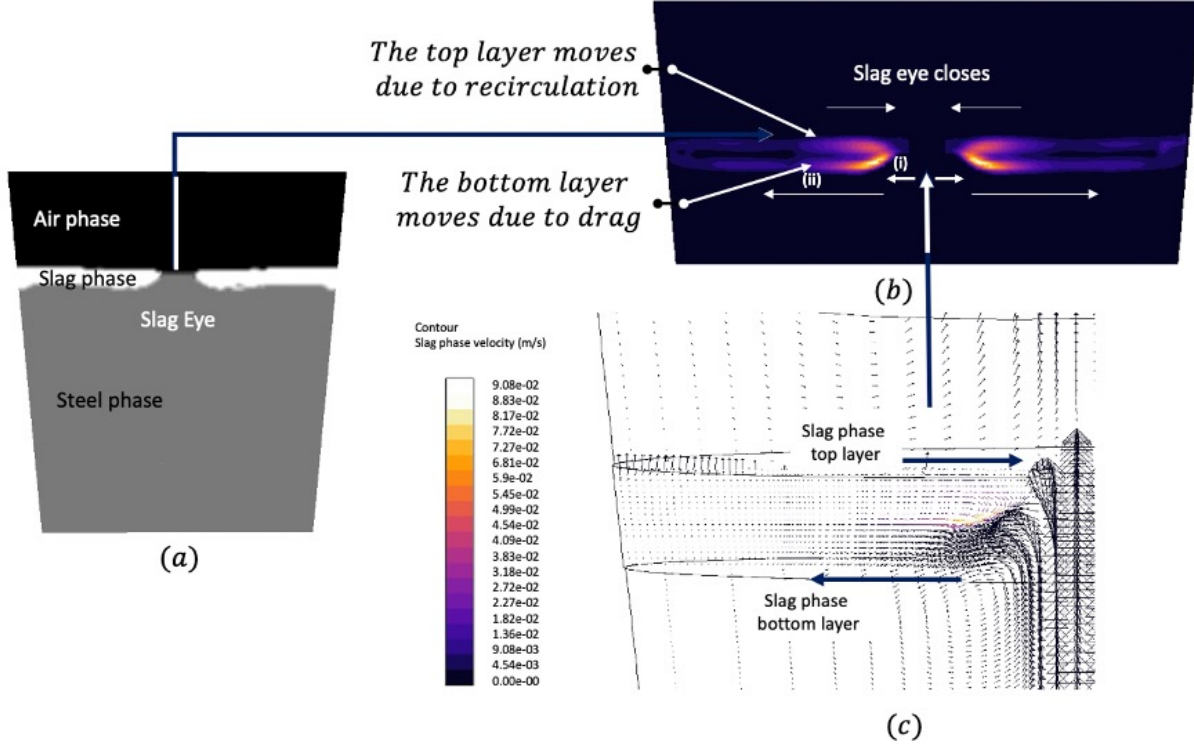


Figure 12: (a) Slag eye build-up during ladle refining operation at an argon flow rate of 400 Lt/min. (b) Process of slag eye closure due to increasing recirculation in the ladle slag colour mapped to slag's velocity magnitude (c) Velocity vector plot of continuous phases (Steel, slag and air) colour mapped to slag's velocity magnitude.

In order to understand the effects of changing thermo-physical properties on the flow behavior of slag. We observe Fig. 13(c), where we have a vector plot of a zoomed ladle in the slag-metal interfacial region. The plot is colour-mapped for the slag phase velocity magnitude. Here we observe an accelerated (changing velocity vector direction) slag phase as a result of the convective drag produced by the adjacent flowing metal phase. Adding to this result the information coming from the thermophysical plot of the slag, we see that the slag region with maximum slag viscosity corresponds to the maximum drag produced in the slag phase and the maximum velocity profile in the slag phase from now on. Here we see that the slope of the slag eye increases, but due to the higher returning fluid due to the increased recirculation, the top part of the eye also closes, and a smaller eye is formed. Furthermore, the slag phase in the vicinity of the open eye is relatively denser than the rest of the slag phase. This creates a gravitational push on the lower region of the slag phase in that region, and accordingly the circulation in the phase which we can see in the figure.

Due to this the circulations in the slag phase increases and an increased circulation then diminishes the slag eye region. And thus a relatively smaller slag-eye is formed, as shown in the Fig. ???. Where a comparison has been shown between sag eye area made by Isothermal and non-isothermal conditions. We observe that the mismatch in the slag eye radius is more prominent at higher purging rates, since at higher purging rates we form a larger slag eye and hence there is a much larger heat loss. This larger heat loss creates a larger temperature drop in the slag phase and thus makes it more viscous and dense. This way the slag eye tends to close to a greater extent as explained by the mechanism discussed in this section.

Effects of slag eye formation in non-isothermal conditions on ladle refining

The evolving thermophysical properties of the slag phase due to non-isothermal flow conditions lead to several phenomena related to the changing flow field conditions as discussed in previous sections. In this section, we attempt to

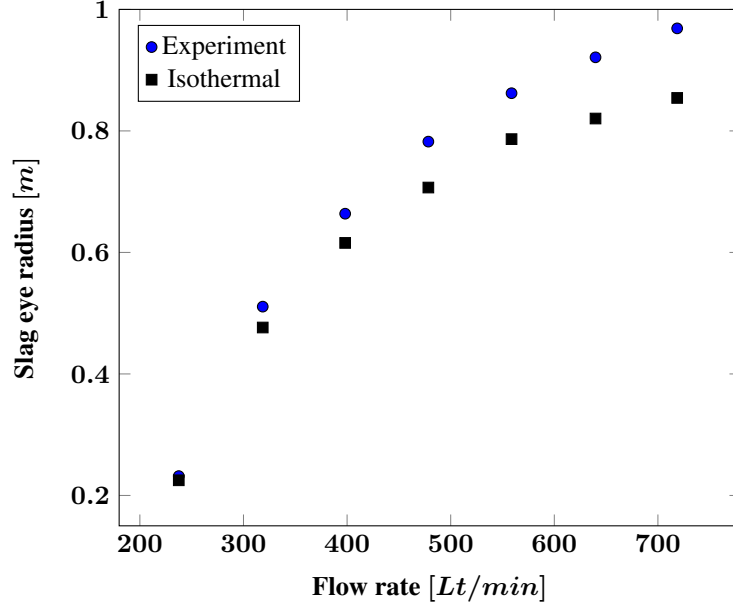


Figure 13: Comparison between normal slag eye area and changing viscosity slag eye area.

analyze its effects on ladle processing. Since the basic purpose of ladle furnaces is to achieve the desired composition values in a given processing time and to facilitate downstream processes such as tundish metallurgy and casting, it is thus important to analyze the impact of this study on interfacial refining reactions. In order to study the effects on interfacial refining reactions, we have used the small eddy mass transfer formulation following the surface renewal principle suggested by Lamont [53]. According to this theory dissipation in the interfacial region due to turbulence in the flow, the field is the main major factor in the mass transfer between the two fluid phases. As shown in Fig. 14(a), we analyze the role of changes in thermophysical properties on changes in disturbance dissipation energy, and further, we explain the steel phase convection mass transfer from this dissipation energy according to Eq. 14., outlined in D6 is correlated.

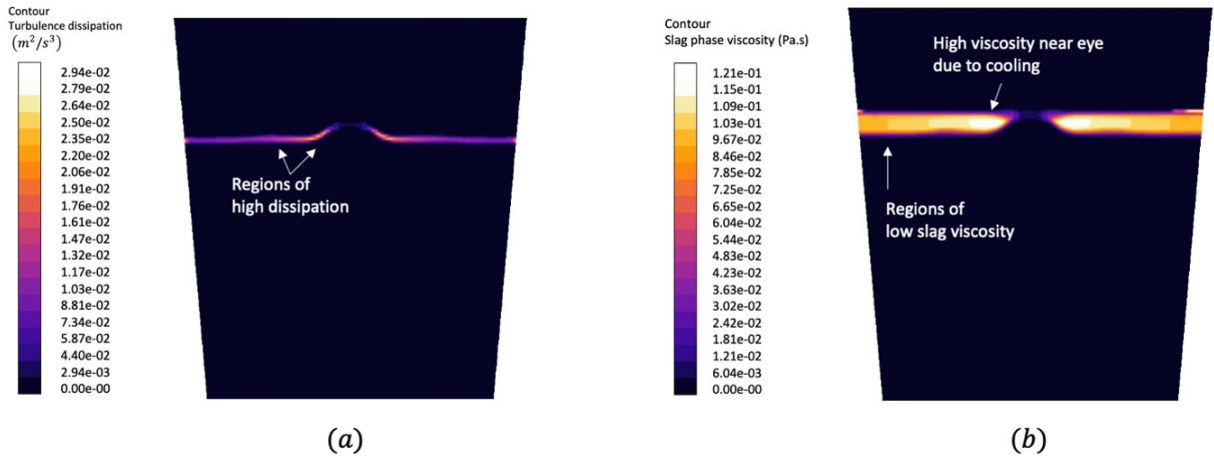


Figure 14: (a) The contour plot of turbulence energy dissipation at the slag metal interface, the contour plane is placed interesting the axis of symmetry. (b) The contour plot of slag viscosity in the ladle.

From Fig. 14(a) and Fig. 14(b) we observe that turbulence energy dissipation is enhanced in the region where the slag's viscosity is lower. Highly viscous slag requires more energy to displace and thus less amount of intermixing is observed in these regions. This is further explained in the context of ladle refining with the help of de-desulfurization of the

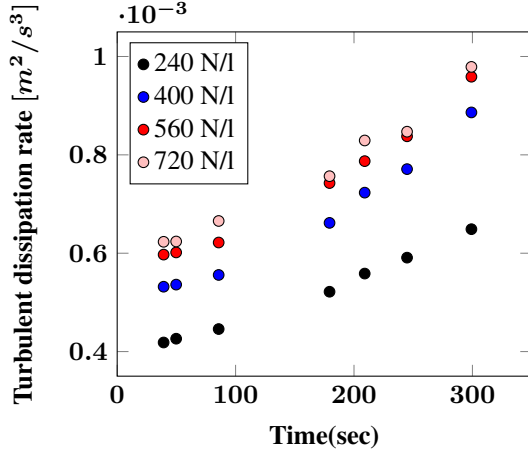


Figure 15: Comparison of dissipation rate

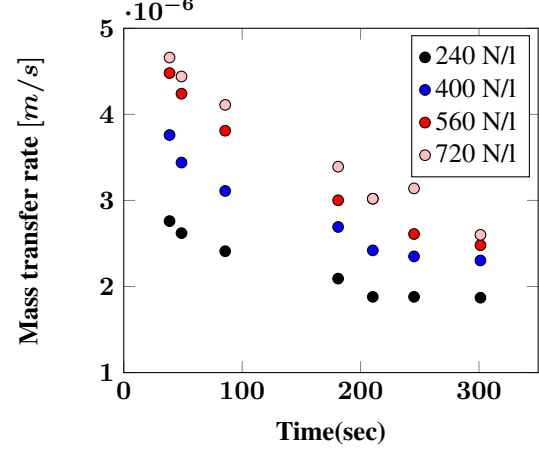


Figure 16: Comparison of mass transfer rate

metal phase. For this, we have defined the turbulent mass transfer of Sulfur between the steel and slag phase at the steel-slag interface. The overall mass transfer coefficient for this process is computed based on the Integration of the mass transfer coefficient expression at the interface as shown in Eq. 16:

$$k_l = \int_{\lim_{f \rightarrow 5}}^{\alpha_{steel} \pm f\% \alpha_{slag} \pm f\%} \left(\frac{\mu}{D} \right)^{-1/2} (\epsilon \mu)^{1/4} dV \quad (16)$$

In Fig. 14(b) we have the viscosity of the slag phase, and we see that the interfacial region has a relatively high viscosity due to the cooling and circulation effect of the slag phase. However, this interface region is constantly exposed to high-temperature molten steel. This high viscosity slag produces high turbulence dissipation of the steel phase turbulent kinetic energy in this region but due to the high slag viscosity, the intermixing in this zone becomes sluggish. As a result, to that, we observe a relatively low slag-metal interfacial area, and thus a decrement in mass transfer coefficient is observed. These results are taken at a fixed sample of time, further, we present the results obtained from transient analysis where non-isothermal cooling of the ladle is taking place. Here, we have presented the evolution of the mass transfer coefficient and turbulent energy dissipation in the lava phase as a function of ladle processing time.

$$[wt\%S(t)] = \int_{De-S\ time} \int_{\lim_{f \rightarrow 5}}^{\alpha_{steel} \pm f\% \alpha_{slag} \pm f\%} K_s \frac{A}{V} \left([wt\%S(t)] - \frac{[wt\%S(t)]}{L_s} \right) dV dt \quad (17)$$

The metal phase Sulfur content is predicted based on the above Eq. 17. Integrating the above equation at the interface we determine the rate of change of the bath's sulfur content and further integrating this rate for the de-sulfurisation time we get the time-dependent sulfur content. In the above equation L_s represents the equilibrium partition coefficient. In our work, we assume L_s to be constant and equal to 350 for the ladle refining conditions. K_s (m/s) represents the mass transfer coefficient for the partitioning of sulfur from metal to slag phase, as derived in the previous section. A/V (m^2/m^3) represents the interfacial area concentration of the interacting slag-metal phases. With the above relation, we can observe the effects of refining with changing argon purging rates.

As seen in Fig. 14(a), we observe that the increasing viscosity increases the dissipation of energy near the interface. As shown in Fig. 15 the argon gas flow rate increases more dissipation can take place near the surface due to increased turbulence. Moreover, with an increasing argon gas flow rate, we expect the slag cooling to take place at a higher rate thus increasing the dissipation. With an increasing dissipation rate, we expect the mass transfer to enhance as per Eq. 16 but we observe some discrepancies with this inference.

The plot of the change in the mass transfer coefficient over time shows that the mass transfer decreases as ladle processing progresses as seen in Fig. 16. The possible explanation for this is attributed to the decrease in the magnitude of the flow in the vicinity of the slag layer due to the increase in the viscosity of the slag layer. Due to the increasing viscosity, more energy is now required to displace the slag layer for slag-metal intermixing and henceforth although the turbulent kinetic energy of dissipation increases, still the mass transfer coefficient decreases in this interfacial region. If such non-isothermal transformations are not considered, the mass transfer and turbulence dissipation turn out to be a

constant value when averaged over time and integrated into space. As the thermophysical slag layer will no longer change with the progress of the refining process. Furthermore, the mass transfer rate tends to decrease at a higher rate at higher argon purging rates. This can be attributed to the higher rate of cooling which can be observed at higher argon purging rates, due to the larger slag eye area. As the slag phases cool down, the higher viscous slag tends to decrease the intermixing of the phases at the interface. This way the refining process will become sluggish.

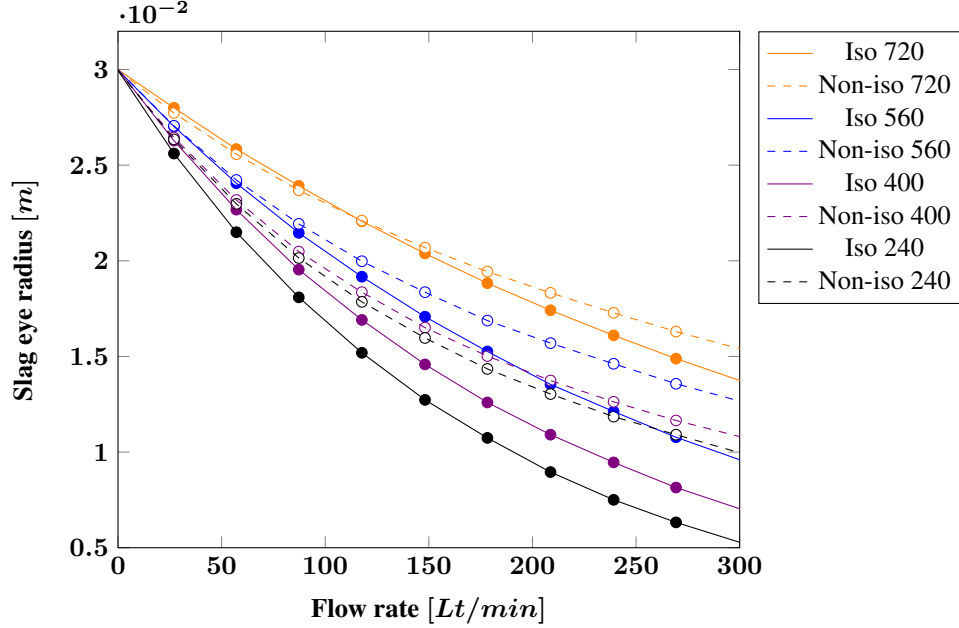


Figure 17: Comparison of the weight percentage content of Sulfur in the molten steel with respect to time during the ladle refining operation in Isothermal and Non-isothermal conditions.

As discussed in the previous section, the non-isothermal conditions during the ladle refining process affect the mass transfer rates of the refining process. Assuming desulfurization to be metal phase mass transfer controlled, and using the formulation as shown in Eq. 17 we solve for the metal phase Sulfur content [%S] with respect to time. From the previous sections, a diminished mass transfer rate leads to a lesser extent of desulfurization from the hot metal.

From Fig. 17, we infer that the final sulfur content decreases as we increase the input argon flow rate. This can be seen due to the increased mass transfer rate at higher argon gas purging rates, as can be seen in Fig. 16. The decrease in final Sulfur content, ΔS [wt.%] between isothermal and non-isothermal models, increases with increasing purging rate increases as we increase the argon flow rate. However, the change in [%S] content between isothermal and non-isothermal conditions increases with time but with a decreasing rate with respect to the argon gas flow rate. This effect can also be inferred from Fig. 16, as the rate of decrement of mass transfer rate increases with increasing purging rates.

6 Conclusion

In this work, a sophisticated multiphase numerical model is implemented on Ansys Fluent. The model involves transient equations of mass, momentum, and energy under turbulent conditions. The discrete particle method is employed to handle the bubble dynamics. Volume of fluid method is employed to track the interface and the radiation is modelled to account for the heat loss from the top surface. The model can study the slag eye formation, intermixing, and refining under non-isothermal conditions. The major conclusions of this work are:

1. The ladle eye opening through which high radiative heat transfer takes place along with the convective cooling, cools down the content of the ladle. Cooling of metal/slag also takes place due to radiation loss from the top and rising gas bubbles. All these results in the change of thermophysical properties, mainly the viscosity of slag.
2. A relatively smaller slag-eye is formed in non-isothermal conditions as compared to the isothermal conditions. The mismatch is more prominent at higher purging rates as a larger slag eye produces a larger temperature

drop in the slag phase and thus makes it more viscous and denser. This way the slag eye tends to close to a greater extent.

3. The results of the slag's kinematic study show the intersection of the high-velocity slag region with higher viscosity region which slows down the slag phase and restricts the bubble plume to grow in radius at the top. This way the slag phase provides greater resistance to slag-eye build-up by the bubble plume.
4. A high argon purging rate corresponds to high turbulent dissipation which corresponds to higher mass transfer rates according to the eddy-dissipation model. But it is also accompanied by a higher degree of slag cooling and increasing viscosity of the slag phase. The net effect of both of these competing effects on mass transfer is observed in the model. Finally, it is concluded that the non-isothermal viscosity changes dominate and thus make the overall mass transfer sluggish.
5. The effects of changing thermophysical properties on ladle refining are concluded by formulating its effect on the mass transfer coefficient of the steel melt. The mass transfer coefficient becomes sluggish as the refining proceeds forward. This decreasing mass transfer rate affects the desulfurization process. Thus to achieve the same level of desulphurization, a non-isothermal case would require more time or higher purging rate compared to an isothermal case.
6. The mass transfer based desulfurisation formulation along with non-isothermal multiphase flow formulation is able to accurately predict metal refining process such as desulphurisation. This validated approach eliminates the necessity of solving computationally intensive equations related to species transport for achieving the same objective.

The work opens up possibilities towards better and more realistic ladle refining optimization. Questions such as optimum argon flow rates in view of competing processing time and unwarranted pick-up of impurities through slag-eye can be effectively addressed. Questions on the extent and need of intermittent arcing during high purging processes like de-sulphurization can also be addressed with the current work.

References

- [1] Lifeng Zhang and Brian G. Thomas. State of the art in evaluation and control of steel cleanliness. *ISIJ International*, 43(3):271–291, 2003. 1
- [2] A. Ghosh. *Secondary Steelmaking: Principles and Applications (1st ed.)*. CRC Press, 2000. 1
- [3] Yongkun Xie and Franz Oeters. Experimental studies on the flow velocity of molten metals in a ladle model at centric gas blowing. *Steel Research*, 63(3):93–104, 1992. 1
- [4] Kimitoshi Yonezawa and Klaus Schwerdtfeger. Spout eyes formed by an emerging gas plume at the surface of a slag-covered metal melt. *Metallurgical and Materials Transactions B*, 30:411–418, 1999. 1
- [5] D. Mazumdar and J.W. Evans. A model for estimating exposed plume eye area in steel refining ladles covered with thin slag. *Metallurgical and Materials Transactions B*, 35:400–404, 2004. 1
- [6] Krishnapisharody Krishnakumar and Gordon A. Irons. An extended model for slag eye size in ladle metallurgy. *ISIJ International*, 48(12):1807–1809, 2008. 1
- [7] L. Wu, P. Valentin, and D. Sichen. Study of open eye formation in an argon stirred ladle. *steel research international*, 81(7):508–515, 2010. 1
- [8] K. Krishnapisharody and G.A. Irons. Modeling of slag eye formation over a metal bath due to gas bubbling. *Metall Mater Trans B*, 37:763–772, 2006. 1, 4
- [9] Z. Liu, L. Li, and B. Li. Modeling of gas-steel-slag three-phase flow in ladle metallurgy: Part 1. physical modeling. *ISIS International*, 57(11):1971–1979, 2017. 1
- [10] Olena Volkova and Dieter Janke. Modelling of temperature distribution in refractory ladle lining for steelmaking. *ISIJ international*, 43(8):1185–1190, 2003. 1
- [11] Ünal Çamdali and Murat Tunc. Steady state heat transfer of ladle furnace during steel production process. *Journal of Iron and Steel Research, International*, 13(3):18–25, 2006. 1
- [12] André Zimmer, Álvaro Niedersberg Correia Lima, Rafael Mello Trommer, Saulo Roca Bragança, and Carlos Pérez Bergmann. Heat transfer in steelmaking ladle. *Journal of Iron and Steel Research, International*, 15(3):11–60, 2008. 1
- [13] D. A. Livshits et al. Heat-loss calculation in ladle treatment of steel. *Steel in Translation*, 40(11):979–982, 2011. 1

- [14] Björn Glaser, Mårten Görnerup, and Du Sichen. Thermal modelling of the ladle preheating process. *steel research international*, 82(12):1425–1434, 2011. 1
- [15] Z. K. Kabakov and M. A. Pakholkova. Reducing the loss of heat from steel in steel-pouring ladles. *Metallurgist*, 56(9):670–671, 2013. 1
- [16] Varadarajan Seshadri, Izabela Diniz Duarte, Itavahn Alves Da Silva, and Carlos Antonio Da Silva. *Evaluation of Heat Flow and Thermal Stratification in A Steelmaking Ladle Through Mathematical Modelling*, chapter 60, pages 487–494. John Wiley & Sons, Ltd, 2016. 1
- [17] J. E. Farrera-Buenrostro et al. Analysis of temperature losses of the liquid steel in a ladle furnace during desulfurization stage. *Transactions of the Indian Institute of Metals*, 72(4):899–909, 2019. 1
- [18] H. Gonzalez et al. Multiphase modeling of fluid dynamic in ladle steel operations under non-isothermal conditions. *Journal of Iron and Steel Research International*, 24(9):888–900, 2017. 1
- [19] Jeong Whan Han et al. Transient fluid flow phenomena in a gas stirred liquid bath with top oil layer—approach by numerical simulation and water model experiments. *ISIJ international*, 41(10):1165–1172, 2001. 1
- [20] Leili Tafaghodi Khajavi and Mansoor Barati. Liquid mixing in thick-slag-covered metallurgical baths—blending of bath. *Metallurgical and Materials Transactions B*, 41(1):86–93, 2010. 1
- [21] W. Liu, H. Tang, S. Yang, et al. Numerical simulation of slag eye formation and slag entrapment in a bottom-blown argon-stirred ladle. *Metall. Mater. Trans. B*, 49:2681–2691, 2018. 1, 3.1
- [22] D. Guo and G. A. Irons. A water model and numerical study of the spout height in a gas-stirred vessel. *Metallurgical and Materials Transactions B*, 33(3):377–384, 2002. 1
- [23] M. Thunman, S. Eckert, O. Hennig, J. Björkvall, and Du Sichen. Study on the formation of open-eye and slag entrainment in gas stirred ladle. *steel research international*, 78(12):849–856, 2007. 1
- [24] Ning ning Lv, Liu shun Wu, Hai chuan Wang, Yuan chi Dong, and Chang Su. Size analysis of slag eye formed by gas blowing in ladle refining. *Journal of Iron and Steel Research, International*, 24(3):243–250, 2017. 1
- [25] P. Valentin et al. Influence of the stirring gas in a 170-t ladle on mixing phenomena—formation and on-line control of open-eye at an industrial ld steel plant. *steel research international*, 80(8):552–558, 2009. 1
- [26] Heping Liu, Zhenya Qi, and Mianguang Xu. Numerical simulation of fluid flow and interfacial behavior in three-phase argon-stirred ladles with one plug and dual plugs. *Steel research international*, 82(4):440–458, 2011. 1
- [27] Baokuan Li et al. Modeling of three-phase flows and behavior of slag/steel interface in an argon gas stirred ladle. *ISIJ international*, 48(12):1704–1711, 2008. 1, 3
- [28] Linmin Li, Zhongqiu Liu, Baokuan Li, Hiroyuki Matsuura, and Fumitaka Tsukihashi. Water model and cfd-pbm coupled model of gas-liquid-slag three-phase flow in ladle metallurgy. *ISIJ International*, 55(7):1337–1346, 2015. 1
- [29] Linmin Li and Baokuan Li. Investigation of bubble-slag layer behaviors with hybrid Eulerian–Lagrangian modeling and large eddy simulation. *JOM*, 68(8):2160–2169, 2016. 1
- [30] Linmin Li, Baokuan Li, and Zhongqiu Liu. Modeling of gas-steel-slag three-phase flow in ladle metallurgy: Part ii. multi-scale mathematical model. *ISIJ International*, (ISIJINT-2017), 2017. 1
- [31] Umesh Singh et al. Multiphase modeling of bottom-stirred ladle for prediction of slag–steel interface and estimation of desulfurization behavior. *Metallurgical and Materials Transactions B*, 47(3):1804–1816, 2016. 1
- [32] Eshwar Kumar Ramasetti et al. Physical and cfd modeling of the effect of top layer properties on the formation of open-eye in gas-stirred ladles with single and dual-plugs. *steel research international*, 90(8):1900088, 2019. 1, 2, 3
- [33] Lage Jonsson and Pär Jönsson. Modeling of fluid flow conditions around the slag/metal interface in a gas-stirred ladle. *ISIJ international*, 36(9):1127–1134, 1996. 1, 9, 4
- [34] Lage Jonsson, Du Sichen, and Pär Jönsson. A new approach to model sulfurrefining in a gas-stirred ladle—a coupled cfd and thermodynamic model. *ISIJ international*, 38(3):260–267, 1998. 1
- [35] Anne-Marie Lejeune and Pascal Richet. Rheology of crystal-bearing silicate melts: An experimental study at high viscosities. *Journal of Geophysical Research: Solid Earth*, 100(B3):4215–4229, 1995. 2, 3.1
- [36] B. E. Launder and D. B. Spalding. *Lectures in Mathematical Models of Turbulence*. Academic Press, London, England, 1972. 2, 3.1

- [37] Dian-Qiao Geng, Hong Lei, and Ji-Cheng He. Numerical simulation for collision and growth of inclusions in ladles stirred with different porous plug configurations. *ISIJ International*, 50(11):1597–1605, 2010. 3
- [38] Carlos A. Llanos, Saul Garcia, J. Angel Ramos-Banderas, Jose de J. Barreto, and Gildardo Solorio. Multiphase modeling of the fluidynamics of bottom argon bubbling during ladle operations. *ISIJ International*, 50(3):396–402, 2010. 3
- [39] Lifeng Zhang. Application of computational fluid dynamics (cf) modeling on the transport phenomena during casting process. *JOM*, 64(9):1059–1062, 2012. 3
- [40] Duan Haojian, Lifeng Zhang, Brian Thomas, and Alberto Conejo. Fluid flow, dissolution, and mixing phenomena in argon-stirred steel ladles. *Metallurgical and Materials Transactions B*, 49, 07 2018. 3
- [41] G. K. Batchelor. *An Introduction to Fluid Dynamics*. Cambridge University Press, Cambridge, England, 1967. 3
- [42] R. Roscoe. The viscosity of suspensions of rigid spheres. *British journal of applied physics*, 3(8):267, 1952. 3, 3.1
- [43] B. D. Marsh. On the crystallinity, probability of occurrence, and rheology of lava and magma. *Contributions to Mineralogy and Petrology*, 78(1):85–98, 1981. 3, 3.1
- [44] Christopher W Bale, Patrice Chartrand, SA Degterov, G Eriksson, K Hack, R Ben Mahfoud, J Melançon, AD Pelton, and S Petersen. Factsage thermochemical software and databases. *Calphad*, 26(2):189–228, 2002. 3.1, 3.1
- [45] A. Sinha. Thesis. Master’s thesis, 2020. 6
- [46] C. L. Rosenberg and M. R. Handy. Experimental deformation of partially melted granite revisited: implications for the continental crust. *Journal of Metamorphic Geology*, 23(1):19–28, 2005. 3.1
- [47] Björn Glaser. *A Study on the Thermal State of Steelmaking Ladles*. PhD thesis, KTH Royal Institute of Technology, 2012. 7
- [48] David C. Wilcox. Reassessment of the scale-determining equation for advanced turbulence models. *AIAA Journal*, 26(11):1299–1310, 1988. 3.1
- [49] P. V. Danckwerts. Significance of liquid-film coefficients in gas absorption. *Ind. Eng. Chem.*, 43(6):1460–1467, 1951. 3.1
- [50] Raad I. Issa, A. D. Gosman, and A. P. Watkins. The computation of compressible and incompressible recirculating flows by a non-iterative implicit scheme. *Journal of Computational Physics*, 62(1):66–82, 1986. 3.1
- [51] Dimitri Mavriplis. Revisiting the least-squares procedure for gradient reconstruction on unstructured meshes. In *16th AIAA Computational Fluid Dynamics Conference*, 2003. 3.1
- [52] ANSYS Inc., USA. *Ansys Fluent Theory Guide*, 2011. 4
- [53] John C. Lamont and D. S. Scott. An eddy cell model of mass transfer into the surface of a turbulent liquid. *AIChE Journal*, 16(4):513–519, 1970. 5.2